

PHYSICAL PROPERTIES OF THE MOLECULAR OUTFLOW IN HIGH-MASS STAR-FORMING REGION G240.31+0.07

JUNHAO LIU and KEPING QIU

School of Astronomy & Space Science, Nanjing University, Nanjing, P.R.China

ABSTRACT

We present low and high angular resolution observations toward outflow gas of massive star forming region G240.31+0.07, with the Submillimeter Array (SMA) and the Caltech Submillimeter Observatory (CSO) 10.4 m telescope in CO (2-1), and with Atacama Pathfinder Experiment (APEX) in CO (3-2), (6-5), and (7-6). Velocity integrated emissions of different transitions show similarity in morphology. With multi-transition CO lines, we find the relationship between outflowing gas temperature and velocity with Large Velocity Gradient (LVG) modeling. Our results reveal that the temperature of the outflowing gas has no obvious dependence on gas velocity, which is consistent with the wide-angle wind model.

Subject headings: ISM: individual (G240.31+0.07) - ISM: jets and outflows - stars: formation - stars: early-type

1. INTRODUCTION

Bipolar molecular outflows are ubiquitous around low-mass and high-mass young stellar objects (Lada 1985; Fukui et al. 1993; Zhang et al. 2001; Beuther et al. 2002; Maud et al. 2015). Theoretical work suggests that, in low-mass star formation, molecular outflows are related to disk-accretion process, and they play an important role in dissipating excess angular momentum of the infalling material (Shu et al. 1987; Bachiller 1996). However, due to the rarity and the typically larger distances, massive molecular outflows and their driving sources are not well studied as their low-mass counterparts. Thus, it is not clear how the massive outflows are accelerated, how they differ from low-mass outflows, and how they affect the star forming process. It is essential to address these questions by studying individual high-mass star forming regions.

Here we study G240.31+0.07 (hereafter G240), an active high-mass star formation region which is associated with the IRAS 07427-2400 source and located at a distance of 5.41 kpc (Sakai et al. 2015). It harbors an ultracompact (UC) HII region and is reported to have OH and H₂O

maser emission (Hughes & MacLeod 1993; Caswell 1997; MacLeod et al. 1998; Migenes et al. 1999; Caswell 2003). Its far-infrared luminosity of $10^{4.7} L_{\odot}$ is consistent with a O8.5 spectral type zero-age main-sequence (ZAMS) star (MacLeod et al. 1998). A near-infrared study have found two bright elongated H₂ emission knots near the source (Kumar et al. 2002). Kumar et al. (2003) further argued that the shocked H₂ emission indicates the presence of a massive rotating disk or envelope around the luminous YSO IRAS 07427-2400. There are also millimeter and centimeter radio continuum observations towards G240. Two clumps were detected by Chen et al. (2007) at 654 GHz (460 μ m), with clump A coinciding with a VLA 6 cm point source (Hughes & MacLeod 1993) and an H₂O maser. Qiu et al. (2009) presented a high resolution interferometric study at 1.3 mm and resolved the central part of G240 into three dusty cores MM1, MM2, and MM3, with the brightest core MM1 coinciding with the VLA 6 cm point source spatially. Trinidad (2011) presented observations at 1.3, 3.6, and 6 cm and reported radio continuum emission at the position of the three millimeter sources in at least one wavelength. G240 have also been mapped with single

dish and interferometric observations in CO emission. High velocity CO (1-0) gas was detected towards G240 (McCutcheon et al. 1991; Shepherd & Churchwell 1996), tracing a bipolar outflow (Shepherd & Churchwell 1996). Hunter (1997) mapped the CO (3-2) emission with a $20''$ beam and found a prominent bipolar outflow at a position angle (PA) of 138° and a weaker component at $PA \approx 101^\circ$. Kumar et al. (2003) also detected the prominent and weaker components of the bipolar CO (3-2) outflow with a $20''$ beam and reported the PA of the prominent component to be 132° . Recently, Qiu et al. (2009) presented a single dish and interferometric study of $12\text{CO}(2-1)$ and $13\text{CO}(2-1)$ emission and detected a bipolar, wide-angle, quasi-parabolic molecular outflow. In addition, Qiu et al. (2014) reported the detection of an hourglass magnetic field aligned within 20° of the outflow axis.

In this paper we present a CO multi transition (2-1, 3-2, 6-5, 7-6) study towards the G240 outflow. With large velocity gradient (LVG) calculations, we explore the physical properties of the outflowing gas as a function of outflow velocity. We then discuss the driven mechanism of the outflow.

2. OBSERVATIONS

The Submillimeter Array¹ (SMA) observations were carried out on 2008 February 25 with eight antennas in the compact configuration and on 2008 February 16 with seven antennas in the extended configuration. To ensure the coverage of the entire outflow we observed two fields centered at (R.A., del.) $_{J2000} = (07^{\text{h}}44^{\text{m}}52^{\text{s}}.49, 24^{\text{d}}07^{\text{m}}52^{\text{s}}.1)$ and (R.A., del.) $_{J2000} = (07^{\text{h}}44^{\text{m}}51^{\text{s}}.07, 24^{\text{d}}07^{\text{m}}34^{\text{s}}.9)$, respectively. We used Titan as the primary flux calibrator and 3c273 as the bandpass calibrator. The time dependent gain was monitored by observing quasars J0730-116 and J0826-225 every 23 minutes. Visibilities were calibrated using the IDLMIR package and then output to MIRIAD for imaging. With natural weighting the synthesized

beams in the compact and extended configurations are about $4'' \times 3''$ and $1''.2 \times 1''$, respectively. The shortest baseline in our SMA observations is 16.5 m, corresponding to a spatial scale of $20''$ for observations at 225 GHz. Thus, spatial structures more extended than $20''$ were not sampled in the SMA observations. This spatial filtering can significantly affect the CO (2-1) maps at velocities close to the cloud velocity. To recover the missing short spacing information we observed the CO (2-1) emission with the Caltech Submillimeter Observatory² (CSO) 10.4 m telescope on 2008 February 12. During the observation the weather condition was excellent for 1 mm waveband with $\tau_{225\text{GHz}} \approx 0.08$. The observations were carried out in the on-the-fly mode centered on (R.A., del.) $_{J2000} = (07^{\text{h}}44^{\text{m}}52^{\text{s}}.1, 24^{\text{d}}07^{\text{m}}49^{\text{s}})$. We obtained a 15×15 grid in CO (2-1), with an integration of about 5 s on each cell. The $10''$ cell spacing is about one-third of the CSO beam, which is $\approx 32''.5$ in CO (2-1). By observing Mars and Saturn we derived a beam efficiency of 0.58–0.10. The spectrometer used has 1024 channels throughout the 50 MHz bandwidth, resulting in a spectral resolution of 0.0488 MHz (about 0.065 km s^{-1}) per channel. The final maps were smoothed to 2 km s^{-1} per channel. The data were reduced using the standard CLASS package. We combined the SMA compact and CSO CO (2-1) data in MIRIAD following a procedure outlined in Zhang et al. (1995).

The 12-m submillimeter Atacama Pathfinder Experiment Telescope³ (APEX) observations were conducted on . CO (6-5) and CO (7-6) were observed simultaneously.

3. RESULTS

3.1. CO EMISSION

Figure 1 shows maps of the integrated low-velocity (LV) and high-velocity (HV) blueshifted and redshifted emissions of CO $J = (3-2), (6-5), (7-6)$ lines. For comparison, we integrate the LV and HV line wings of CO (3-2) and CO (6-5), as well as CO (7-6) LV emission, with the same ve-

¹The Submillimeter Array is a joint project between the Smithsonian Astrophysical Observatory and the Academia Sinica Institute of Astronomy and Astrophysics and is funded by the Smithsonian Institution and the Academia Sinica.

²The Caltech Submillimeter Observatory was supported by the NSF grant AST-0229008 and was closed on September 18, 2015.

³APEX is a collaboration between the Max-Planck-Institut für Radioastronomie, the European Southern Observatory, and the Onsala Space Observatory.

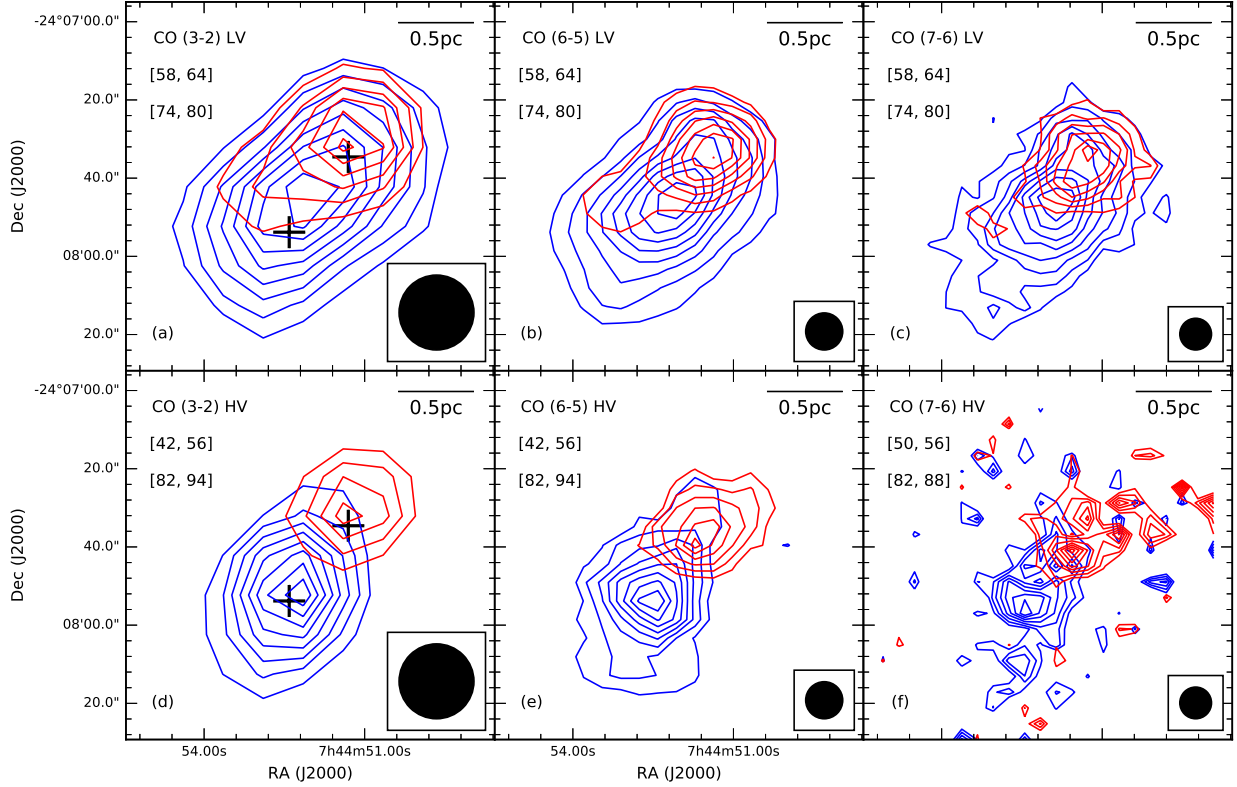


Fig. 1.— (a)-(c) Low-velocity emission of CO $J = (3-2)$, $(6-5)$, $(7-6)$ lines, with velocity range 58 to 64 km s⁻¹ and 74 to 80 km s⁻¹ for the blueshifted lobe (blue) and the redshifted lobe (red); (d)-(e) High-velocity emission of CO $J = (3-2)$, $(6-5)$ lines, with velocity range 42 to 56 km s⁻¹ and 82 to 94 km s⁻¹ for the blueshifted lobe (blue) and the redshifted lobe (red); (f) High-velocity CO $J = (7-6)$ emission, with velocity range 50 to 56 km s⁻¹ and 82 to 88 km s⁻¹ for the blueshifted lobe (blue) and the redshifted lobe (red). For (a)-(e), the contour levels are starting from 20% and at steps of 10%. For (f), the contour levels are starting from 30% and at steps of 10%. The central stars mark the position of the millimeter sources detected by Qiu et al. (2009). The beam size is shown in the lower right corner of each panel.

locity range as Qiu et al. (2009) Figure 2 (a) and Figure 2 (b), which is 58 to 64 km s⁻¹ and 74 to 80 km s⁻¹ for the LV blueshifted lobe and redshifted lobe, 42 to 56 km s⁻¹ and 82 to 94 km s⁻¹ for the HV blueshifted lobe and redshifted lobe. As CO (7-6) observation is less sensitive than observations of CO (3-2) and CO (6-5), we integrate the HV emission of CO (7-6) with 50 to 56 km s⁻¹ for the blueshifted lobe and 82 to 88 km s⁻¹ for the redshifted lobe, to exclude channels which are dominated by noise. For CO J = (3-2) and (6-5) emissions, a low-velocity and high-velocity prominent bipolar outflow is detected at position angle (PA) $\approx 131^\circ$, along with a low-velocity weaker component detected at PA $\approx 101^\circ$. However, the weaker outflow is not clearly seen in CO (7-6). It could result from the limited sensitivity of CO (7-6) observation. And, due to lower resolution of our CO J = (3-2), (6-5), (7-6) observations, we don't see the wide-angle structure reported by Qiu et al. (2009).

3.2. LINE RATIOS

With multi transition CO lines observation, it is feasible to estimate the physical parameters of the outflowing and investigate their velocity dependence by means of statistical-equilibrium calculations. For a proper comparison, we reconstructed CO (2-1), (6-5) and (7-6) data to the same spatial resolution of CO (3-2), which is 19''.16. To reduce the noise level, we resampled the spectra of four CO lines to a resolution of 2 km s⁻¹. Then we measured the main beam temperature ratios of the four transitions toward the peak of the blueshifted and redshifted lobes (marked as two crosses in Figure 1). We adopted the cloud velocity (v_{cloud}) from Kumar et al. (2003), which is about 67.5 km s⁻¹ with respect to the local standard of rest. Figure 2 shows the ratio-velocity distributions of the blueshifted gas and redshifted gas. The plot exhibits that all line ratios ((7-6)/(6-5), (6-5)/(3-2), (6-5)/(2-1)) keep almost unchanged with the increase of outflow velocity, thus indicating the homogeneity within the outflowing gas.

3.3. PHYSICAL PROPERTY ANALYSIS

We performed LVG analysis with the radiative transfer code RADEX developed by van der Tak et al. (2007). The simulation constructs a large

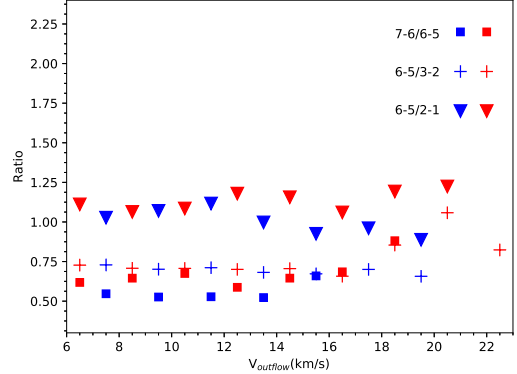


Fig. 2.— Ratios of main beam temperature of different CO lines versus outflowing gas velocity, as observed towards the blueshifted lobe (blue symbols) and the redshifted lobe (red symbols). The V_{outflow} shown here is the gas velocity with respect to the cloud velocity (v_{cloud}): $V_{\text{outflow}} = |v_{\text{observed}} - v_{\text{cloud}}|$, where v_{observed} is the observed gas velocity.

grid of non-LTE models with three parameters: gas density (n_{H_2}), kinetic temperature (T_{kin}), and the ratio between column density and line width ($N_{\text{CO}}/\Delta V$). Considering of the velocity resolution of our observations, we fix ΔV to 2 km s⁻¹. Each model gives the prediction of the brightness temperature (T_{b}) of different CO transitions. With CO line datas resampled and reconstructed, we measured main beam temperature (T_{mb}) of the four CO lines extracted at the peak position of the blue lobe and red lobe (marked as two crosses in Figure 1). To compare the simulated T_{b} with our measured T_{mb} , we need to consider about the beam dilution, as T_{mb} is related to T_{b} :

$$T_{\text{mb}} = \frac{\Omega_{\text{s}}^2}{\Omega_{\text{s}}^2 + \Omega_{\text{mb}}^2} \times T_{\text{b}} = \eta_{\text{b}} \times T_{\text{b}}, \quad (1)$$

where Ω_{s} and Ω_{mb} are the source size and the beam size in arcsec, and η_{b} is the beam filling factor. Given the complex structures of G240 outflow at higher resolution (Qiu et al. 2009), we can't get a good estimate of the source size. Then the beam filling factors are assumed to be the same for all transitions, and fixed to 1, during our analysis. Thus, the derived physical parameters of the gas are beam-averaged values. We further discuss how

the beam dilution affect our results in the belowing part of this section.

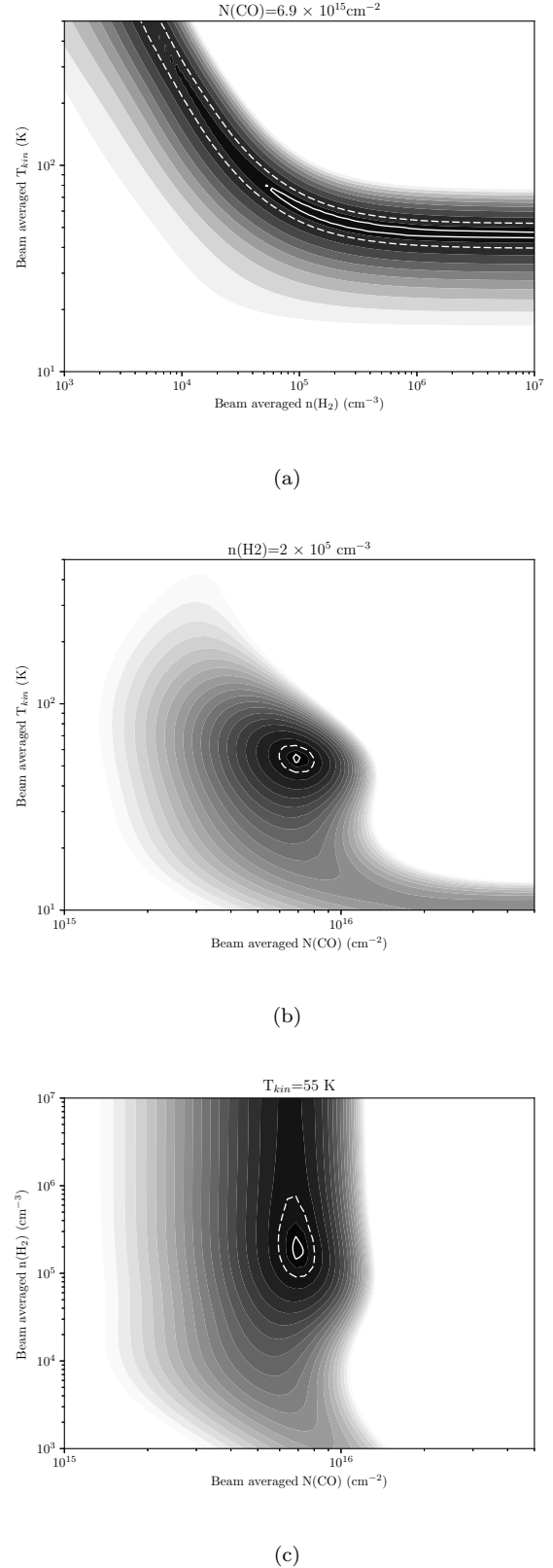
We report the results from a χ^2_{red} fitting. χ^2_{red} is the reduced χ^2 :

$$\chi^2_{\text{red}} = \frac{1}{N - n} \sum_{i=1}^4 (I_o - I_m)^2 / \sigma^2, \quad (2)$$

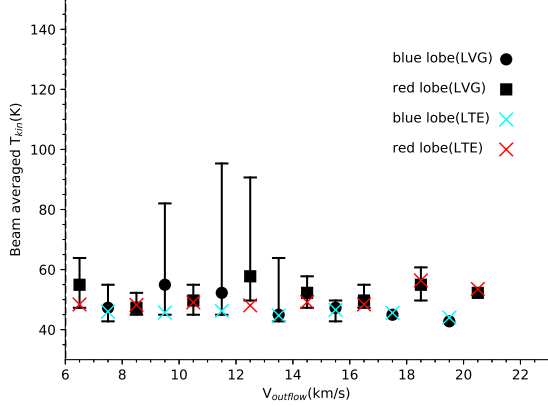
where N is the number of observed intensities, n the number of fitted parameters, I_o the observed intensity, I_m the modelled intensity, and σ , the uncertainty of the observed intensity. With four lines observations and three simulation parameters, our fitting has one degrees of freedom. Considering the calibration error and pointing accuracy of our CO observations, we set the intensity uncertainty of CO (2-1), CO (3-2), CO (6-5), CO (7-6) to 0.15, 0.2, 0.25, 0.3 respectively. The best fit is then obtained by minimizing the χ^2_{red} between the observed and modelled data using the Levenberg-Marquardt method (Press et al. 1992). However, in velocities where no CO (7-6) emission is detected, the best fit is obtained by minimizing χ^2 instead of χ^2_{red} . Then we found the best fitting result at most velocities has a χ^2_{red} less than 1, indicating that we might be a bit conservative at the intensity uncertainty. So we divided the intensity uncertainties by a appropriate factor to make χ^2_{red} approach 1 at most velocities. At some velocities, the χ^2_{red} remains much less than 1 even after our adjustment of intensity uncertainty, which can accounts for the anomaly high upper limits of gas temperature at these velocities in Figure 4(a).

In Figure 3, we show cuts in the χ^2_{red} along the $[T, n]$, $[T, N]$, $[n, N]$ planes for 58 km s⁻¹ as examples of the χ^2_{red} distribution, with all other parameters fixed to the parameters of the best fitting results at this velocity. The χ^2_{red} distribution in $[T, n]$, $[T, N]$ planes is well behaved, with only one minimum, as shown in Figure 3(b) and Figure 3(c). However, Figure 3(a) shows that the gas might be thermalised and no upper limits to the density could be derived. The χ^2_{red} distribution behaves similarly at other velocities.

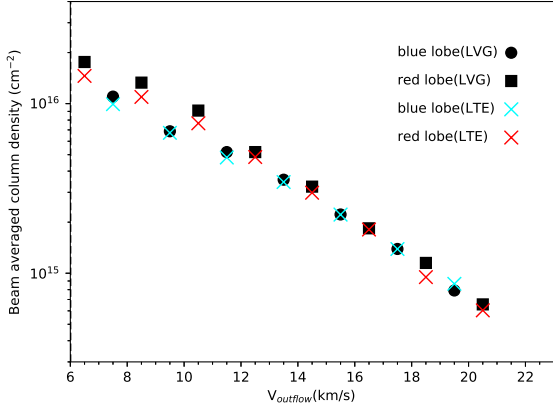
We also performed a population diagram analysis with the assumption of local thermal equilibrium (LTE) and optically thin, and derived the kinetic temperature of the outflow gas and the CO column density as a function of velocity (Goldsmith & Langer 1999). Figure 4 shows the out-



5 Fig. 3.— The χ^2_{red} distribution for G240 outflow at 58 km s⁻¹ in the (a) $[T, n]$, (b) $[T, N]$, (c) $[n, N]$ planes, with all other parameters fixed to the parameters of the best fitting results at this velocity. Solid contours and dashed contours show the 1 σ and 3 σ confidence levels respectively.



(a)



(b)

Fig. 4.— T - V and N - V diagram of the G240 outflow, estimated from LVG analysis (black circles for blue lobe and black squares for red lobe) and population diagram analysis (cyan x marker for blue lobe and red x marker for red lobe). The 1σ temperature uncertainty estimated from the LVG analysis is represented in the T - V diagram (error bars).

flowing gas temperature and CO column density, estimated from the LVG analysis and population diagram analysis, versus outflowing gas velocity. The N - V diagram exhibits a clear decreasing trend of CO column density with outflow velocity, while the T - V diagram shows that the gas temperature has no obvious dependence on gas velocity. Uncertainty of each parameter in the LVG analysis is derived from the 1σ confidence region in the N - T - n 3-dimensional space. The 1σ temperature uncertainty of the LVG analysis is shown in Figure 4(a), at velocities where all of the four lines are detected. The uncertainty of the CO column density is too small to be plotted, so we don't show it in Figure 4(b). The lower limit of gas density is around $10^4 - 10^5 \text{ cm}^{-3}$ for all velocities.

To explore how the effect of beam dilution influence our results, we varied the beam filling factors from 0.3 to 1. Then we performed the LVG analysis again, and compared the simulated T_b with the corrected antenna temperatures (T_{mb} divided by a beam filling factor). We find that modelling with different beam filling factors mainly affect the N - V diagram, with minor change in the T - V diagram and density limits, which could be resulted from the degeneracies of the beam filling factor with CO column density in the optically thin case.

4. DISCUSSION

With priori assumption of other parameters, the kinetic temperature of the outflowing gas can be derived from LVG analysis using two CO lines. A rising trend of CO 3-2/6-5 ratio is observed towards the outflow gas associated with low mass YSO HH46 (van Kempen et al. 2009). If the density remains constant, the rising ratios observed at more extreme velocities could correspond to lower kinetic temperatures. In the case of outflowing gas toward low mass protostars NGC 1333 IRAS 4A and IRAS 4B, the CO 3-2/6-5 ratios are remarkably constant with velocity (Yildiz et al. 2012). With the assumption of constant density, the constant ratio trend shows little or no evidence of a temperature change with velocity. Based on CO (2-1) and CO (3-2) observations towards the extremely high velocity outflow of high mass YSO G5.89-0.39, Su et al. (2012) assumed the canonical CO fractional abundance of 10^{-4} and performed a LVG analysis, revealing a increasing trend of

temperature with gas velocity. However, using the CO (6-5), (7-6) and (16-15) lines, Leurini et al. (2015) performed a rotation diagram analysis towards G5.89-0.39 outflow and found a decreasing trend of temperature with increasing velocities. This disagreement seen in results of Su et al. (2012) and Leurini et al. (2015) could be due to different angular resolutions ($3''.4$ compared to $14''.5$). While Su et al. (2012) has smaller energy range covered by their CO line observations ($\Delta E_u \sim 17$ K) compared to $\Delta E_u \sim 600$ K of Leurini et al. (2015), the decreasing trend of temperature with velocity constrained in Leurini et al. (2015) is probably more appropriate for the G5.89-0.39 outflow. The different distributions of temperature with velocity reveal the complexity of molecular outflows.

In the wide-angle wind model, a molecular outflow is ambient material swept-up by a wide-angle radial wind. In previous numerical works, many authors have chosen isothermal equations for this model (Li & Shu 1996; Lee et al. 2001). Molecular cooling dominates the cooling of the shocked material in the outflow at temperatures below 10^4 K (Hollenbach 1997). As the cooling rate increases as n^2 , molecular cooling is very efficient for the density of a wind-driven outflow. Thus, an isothermal state could be reached in a wind-driven outflow, with no temperature change with velocity. This is consistent with our derivation of almost constant temperature in the massive G240 outflow. In addition, some other features of the molecular outflow associated with G240 can also be qualitatively interpreted by the wide-angle wind model (Qiu et al. 2009), while other outflow models have different predictions of these features, as reviewed by Arce et al. (2007). However, most outflow models existed have parameters typical of low mass outflows. It is necessary to compare the observational results of high mass outflows with models of similar physical conditions. Statics of outflows associated with high mass star forming regions are also essential for us to better understand the driven mechanism of massive outflows and the forming process of high mass stars.

5. SUMMARY

REFERENCES

- Arce, H. G., Shepherd, D., Gueth, F., et al. 2007, *Protostars and Planets V*, 245
- Bachiller, R. 1996, *ARA&A*, 34, 111
- Beuther, H., Schilke, P., Sridharan, T. K., et al. 2002, *A&A*, 383, 892
- Caswell, J. L. 1997, *MNRAS*, 289, 203
- Caswell, J. L. 2003, *MNRAS*, 341, 551
- Chen, H.-R., Su, Y.-N., Liu, S.-Y., et al. 2007, *ApJ*, 654, L87
- Fukui, Y., Iwata, T., Mizuno, A., Bally, J., & Lane, A. P. 1993, *Protostars and Planets III*, 603
- Goldsmith, P. F., & Langer, W. D. 1999, *ApJ*, 517, 209
- Hollenbach, D. 1997, *Herbig-Haro Flows and the Birth of Stars*, 182, 181
- Hughes, V. A., & MacLeod, G. C. 1993, *AJ*, 105, 1495
- Hunter, T. R. 1997, *Ph.D. Thesis*, 238
- Kumar, M. S. N., Bachiller, R., & Davis, C. J. 2002, *ApJ*, 576, 313
- Kumar, M. S. N., Fernandes, A. J. L., Hunter, T. R., Davis, C. J., & Kurtz, S. 2003, *A&A*, 412, 175
- Lada, C. J. 1985, *ARA&A*, 23, 267
- Lee, C.-F., Stone, J. M., Ostriker, E. C., & Mundy, L. G. 2001, *ApJ*, 557, 429
- Leurini, S., Wyrowski, F., Wiesemeyer, H., et al. 2015, *A&A*, 584, A70
- Li, Z.-Y., & Shu, F. H. 1996, *ApJ*, 472, 211
- MacLeod, G. C., Scalise, E., Jr., Saedt, S., Galt, J. A., & Gaylard, M. J. 1998, *AJ*, 116, 1897
- Maud, L. T., Moore, T. J. T., Lumsden, S. L., et al. 2015, *MNRAS*, 453, 645

- McCutcheon, W. H., Sato, T., Dewdney, P. E., & Purton, C. R. 1991, *AJ*, 101, 1435
- Migenes, V., Horiuchi, S., Slysh, V. I., et al. 1999, *ApJS*, 123, 487
- Press, W. H., Teukolsky, S. A., Vetterling, W. T., & Flannery, B. P. 1992, Cambridge: University Press, —c1992, 2nd ed.,
- Qiu, K., Zhang, Q., Wu, J., & Chen, H.-R. 2009, *ApJ*, 696, 66
- Qiu, K., Zhang, Q., Menten, K. M., et al. 2014, *ApJ*, 794, L18
- Sakai, N., Nakanishi, H., Matsuo, M., et al. 2015, *PASJ*, 67, 69
- Shepherd, D. S., & Churchwell, E. 1996, *ApJ*, 457, 267
- Shu, F. H., Adams, F. C., & Lizano, S. 1987, *ARA&A*, 25, 23
- Su, Y.-N., Liu, S.-Y., Chen, H.-R., & Tang, Y.-W. 2012, *ApJ*, 744, L26
- Trinidad, M. A. 2011, *AJ*, 142, 147
- van der Tak, F. F. S., Black, J. H., Schöier, F. L., Jansen, D. J., & van Dishoeck, E. F. 2007, *A&A*, 468, 627
- van Kempen, T. A., van Dishoeck, E. F., Güsten, R., et al. 2009, *A&A*, 501, 633
- Yıldız, U. A., Kristensen, L. E., van Dishoeck, E. F., et al. 2012, *A&A*, 542, A86
- Zhang, Q., Ho, P. T. P., Wright, M. C. H., & Wilner, D. J. 1995, *ApJ*, 451, L71
- Zhang, Q., Hunter, T. R., Brand, J., et al. 2001, *ApJ*, 552, L167